A&A 455, 539–547 (2006)
DOI: 10.1051/0004-6361:20054388

Astronomy & Astrophysics

Hα line profiles for a sample of supergiant HII regions

I. The main spectral component

M. Rozas[1], M. G. Richer[1], J. A. López[1], M. Relaño[2], and J. E. Beckman[3,4]

[1] Instituto de Astronomía, Universidad Nacional Autónoma de México, Ensenada, México
e-mail: maite@astrosen.unam.mx
[2] Facultad de Facultad de Física Teórica y del Cosmos, Universidad de Granada, Spain
e-mail: mrelano@ugr.es
[3] Instituto de Astrofísica de Canarias, La Laguna, Tenerife, Spain
e-mail: jeb@iac.es
[4] Consejo Superior de Investigaciones Cientificas, Spain

Received 20 October 2005 / Accepted 26 April 2006

ABSTRACT

We present an analysis of the Hα emission line profiles of a sample of giant extragalactic HII regions, selected from among the brightest and most isolated in a group of spiral galaxies for which we have photometric and spectroscopic data: NGC 157, NGC 3631, NGC 6764, NGC 3344, NGC 4321, NGC 5364, NGC 5055, NGC 5985, NGC 7479. Our study confirms that the majority of the line profiles are composed of a bright, main component and two fainter, high velocity components that we denominate wings. Here, we analyze the kinematics of the principal components, finding a relation between the Hα luminosity, $L_{\mathrm{H}\alpha}$, and the turbulent velocity dispersion, σ_{nt}. A linear fit to the relation between these quantities yields $\log L_{\mathrm{H}\alpha} = (35.6 \pm 0.4) + (2.87 \pm 0.2) \log \sigma_{\mathrm{nt}}$, in agreement with previous studies. We compute the mass of each HII region using both the virial theorem and the Hα luminosity, confirming that, though these estimates do not coincide exactly, they are comparable within the uncertainties and consequently that the HII regions in our sample are approximately virialized.

Key words. ISM: HII regions – ISM: kinematics and dynamics

1. Introduction

The internal kinematics of HII regions, derived from the line widths of their emission lines and the presence of multiple components, have been the subject of various studies since the 1970's. In particular, whether the large line widths reflect the virialization of the matter in these HII regions has been studied extensively. If so, the line widths can be used to determine the mass of the HII regions. We note at the outset that our objective *is not* to argue that virial equilibrium always determines the kinematic properties of HII regions. Rather, it is unlikely that this condition holds exactly at any time during the evolution of HII regions due to the input of radiative and mechanical energy, principally from their ionizing stars (e.g., Castor et al. 1975). Nonetheless, the least evolved HII regions may well be within a factor of a few (2–3) of having their kinematics determined by their virial masses. At such an early stage, the stellar ionizing luminosities are maximized whereas the mechanical energy input is minimized (e.g., Leitherer et al. 1999). With time, energy input will certainly drive the ionized gas away. Presumably, it is this process that limits the efficiency of star formation (e.g., Kennicutt 1998). In the case of HII regions close to virial equilibrium, the use of the linewidth to compute gaseous masses is a useful, relatively direct means to study their properties since it is independent of the small-scale structure (density, filling factor, etc.).

Smith & Weedman (1970) found that the widths of emission lines in some giant HII regions imply the existence of supersonic motions, which cannot result exclusively from ionizing stellar radiation. Subsequent observations of integrated line profiles in giant HII regions confirmed that these violent internal motions are characteristic of these HII regions (Hippelin 1986; Roy et al. 1986). In the case of extragalactic HII regions, Castañeda et al. (1990) found that the non-thermal contribution significantly exceeded the sound speed in the gas. Melnick (1977) found a correlation between the sizes and Hα luminosities of giant HII regions in late-type spirals using F-P interferometric techniques. He explained this correlation as a result of the velocity dispersions of giant HII regions being a reflection of the stellar velocities within their OB associations. Later, Terlevich & Melnick (1981), in a study based upon Hβ emission, explain the observed line widths as the result of the velocity dispersion of individual clouds of ionized gas moving within the gravitational potential of the gas and stars, according to the virial theorem. In this view, the gas clouds would be overrun by the ionizing stars and the superposition of their individual emission lines along the line of sight and over the resolution element to produce a supersonic line profile. Terlevich & Melnick (1981) claimed to find that the Hβ luminosity of the most luminous HII regions varies as the 4th power of the measured velocity dispersion. They believed that this result showed that the most luminous HII regions are virialized, so that information about their masses, and the resultant mass-luminosity relation, could be obtained using the virial theorem. They also claimed a relation between a radius parameter R and the square of the velocity dispersion σ for HII regions, as further evidence for virialization. However in one of the few complete

statistical studies of velocity dispersions in HII regions within any galaxy, Arsenault et al. (1990) gave observational results for NGC 4321 that in no way approximate to a 4th power relation between L and σ. Their results are more correctly termed a pure scatter diagram, in which the velocity dispersion does not even rise systematically with increasing HII region luminosity.

Other studies have discarded the idea of the virialization of HII regions in favour of other explanations for the L–σ relation; uncertainties in the temperatures and radii of the HII regions as well as asymmetry or multiple components in the line profiles all complicate the fitting of the width with a single Gaussian component (Skillman & Balick 1984; Gallagher & Hunter 1983; Roy et al. 1986; Hippelin et al. 1986; Arsenault & Roy 1988). Some of these studies indicate that the L–σ relation depends upon metallicity, which will lead to erroneous results if a single temperature is adopted to compute the thermal broadening for the entire sample.

Rozas et al. (1998) undertook a study of the entire HII region population in NGC 4321, analyzing the line profiles of its 200 brightest HII regions. In this case, the spectra of each HII region was fit with one or more Gaussian components. The velocity dispersions were analyzed without finding an L–σ relation, but instead a lower envelope to σ in the L–σ plane populated by HII regions that were approximately virialized. The slope of this lower envelope in the L–σ plane was 2.6, not 4 as predicted by the virial theorem, but, as shown by Beckman et al. (2000), HII regions with the largest luminosities are generally density-bounded, which means that a significant fraction of the ionizing radiation escapes and so does not contribute to the luminosity, making shallower slopes physically possible. Two conclusions were drawn from this work. Firstly, the hypothesis about the virialization of the HII regions on the L–σ envelope is vindicated and, secondly, it can be inferred that the masses within an HII region near the envelope is entirelly, in ionized gas: there is no significant contribution from, for example, low mass stars which could not be detected directly.

In a recent study, Relaño et al. (2005) analyze the integrated line profiles of the HII region populations in three spiral galaxies, NGC 1530, NGC 3359, and NGC 6951. They find a lower envelope for the principal components in the L–σ plane with a slope of 2.0. Comparing the masses derived from the virial theorem and from the Hα luminosities, they conclude that the HII regions near the lower envelope are approximately in virial equilibrium whereas HII regions farther from this envelope have velocity dispersions that contain significant contributions from other processes that affect their kinematics and are farther from equilibrium.

Here, we have chosen a sample of 43 HII regions from among the brightest and most isolated in 10 spiral galaxies for which we have photometric and spectroscopic data (NGC 157, NGC 925, NGC 3631, NGC 6764, NGC 3344, NGC 4321, NGC 5364, NGC 5055, NGC 5985 y NGC 7479). We analyze their line profiles, the resulting velocity dispersions, and the L–σ relation using data from a single instrument with higher spectral resolution than used to date in similar studies and analyze all of the data in a homogeneous way. We minimize the errors in the radii adopted for the HII regions by computing them according to a single criterion based upon our own HII region catalogues. Furthermore, we determine the optimum number of Gaussian components to fit to each line profile in order to minimize the uncertainty in the velocity dispersion of the principal component that comprises the majority of the luminosity in each HII region. In a subsequent study, we shall analyze the fainter, secondary components, with higher velocities than the main components.

We remind the reader that our sample is deliberately chosen to include only the intrinsically brightest HII regions that exist (compare with Roberts & Haynes 1994). These are likely to host the youngest, most massive normal star clusters (excluding super star clusters), in which case the processes available to drive the HII region away from virial equilibrium are minimized. Indeed, extant observations, noted above (e.g., Rozas et al. 1998), clearly demonstrate that only a small fraction of all HII regions may be near virial equilibrium. It is only in this small subsample that the line widths may be used to compute their masses approximately.

2. Observations

2.1. Photometric data

The global properties of the galaxies from which our HII region sample is drawn are given in Table 1.

The Hα images of NGC 157, NGC 925, NGC 3631, NGC 4321, NGC 6764 y NGC 7479 were obtained with the 4.2 m William Hershel Telescope at the Observatorio del Roque de los Muchachos on the island of La Palma. The procedures used to reduce the data, calibrate it, and construct the catalogues of HII regions are discussed in Rozas et al. (1996a) for NGC 157, NGC 3631, and NGC 6764, in Rozas et al. (1999) for NGC 7479, in Knapen (1998) for NGC 4321, and in Rozas & Richer (2006, in preparation) for NGC 925.

NGC 3344, NGC 5364, NGC 5055 y NGC 5985 were observed with the 2.1 m telescope of the Observatorio Astronómico Nacional in San Pedro Mártir (OAN-SPM), Baja California, Mexico during 2001 June 29–30. The observing conditions were photometric with the image quality between 1.5″ and 1.6″. The light was filtered with interference filters 20 Å wide centered on the redshifted Hα emission line for each galaxy. Continuum subtraction was accomplished using R-band images. The total integration times were 2×1500 s for the Hα images and 900 s for the R-band images. The images were reduced using standard procedures within the IRAF[1] data reduction package. The bias was subtracted from each image before dividing by the flat field and subtracting a constant value corresponding to the sky background. Field stars were used to align the line and continuum images. Cosmic rays were found and eliminated. The continuum was subtracted from the line images, scaling the images using the relative fluxes of field stars in each image. The scale factor was found to vary between 0.021 and 0.024, depending upon the object (and filter) with the standard deviations within individual images of about 0.004. The uncertainty in the Hα fluxes of the selected HII regions (the brightest) due to the uncertainty in the scale factor is about 3%. The calibration to absolute flux was achieved using observations of spectrophotometric standards from Oke (1990). In Table 2, the Hα luminosity corresponding to a single count is given along with the other data related to the observations.

2.2. Spectroscopic data

High resolution spectroscopic observations of the selected HII regions were obtained using the Manchester Echelle Spectrograph at the 2.1 m telescope of the OAN-SPM (MES, Meaburn et al. 1984, 2003). The MES is a long slit échelle spectrograph without cross dispersion. An interference filter is used

[1] IRAF is distributed by the National Optical Astronomy Observatories, which are operated by the Association of Universities for Research in Astronomy, Inc., under cooperative agreement with the National Science Foundation.

Table 1. Basic parameters of the galaxies.

	NGC 157	NGC 925	NGC 3344	NGC 3631	NGC 4321
RA (2000)	$00^h34^m46^s.5$	$02^h27^m16^s.8$	$10^h43^m30^s.8$	$11^h21^m02^s.7$	$12^h22^m55^s.2$
Dec (2000)	−08 23′48″	+33 34′ 41″	+24 55′25″	+53 10′17″	+15 49′23″
Type	.SXT4..	.SXS7..	RSXR4..	.SAS5..	.SXS4..
log d_{25}	2.10	2.02	1.85	1.70	1.87
B_T	9.31	10.69	10.45	11.01	10.05
v_{opt}	1668	562	575	1143	1579
D (Mpc)	22.2	7.5	7.6	15.2	21.0
log r_{25}	0.24	0.25	0.04	0.02	0.07
	NGC 5055	NGC 5364	NGC 6764	NGC 5985	NGC 7479
RA (2000)	$13^h15^m49^s.3$	$13^h56^m12^s.0$	$19^h08^m16^s.7$	$15^h39^m37^s.8$	$23^h04^m57^s.1$
Dec (2000)	+42 02′06″	+05 00′55″	+50 55′54″	+59 19′57″	+12 19′18″
Type	.SAT4..	.SAT4P.	.SBS4..	.SXR3..	.SBS5..
log d_{25}	2.10	1.83	1.36	1.74	1.61
B_T	9.31	11.17	12.56	11.67	11.60
v_{opt}	516	1267	2412	2520	2394
D (Mpc)	6.8	16.9	32.1	33.6	31.9
log r_{25}	0.24	0.19	0.25	0.02	0.12

Table 2. Hα imaging data and other calibrating parameters.

Galaxy	″/pix	Filter (Hα)	Filter (cont)	Seeing	Calibration constant (erg s^{-1} count^{-1})
NGC 157	0.28	6601/15 Å	6565/15 Å	0.″8	1.47×10^{34}
NGC 925	0.56	6601/15 Å	6565/15 Å	1.″0–1.″2	1.81×10^{34}
NGC 3344	0.59	6576/20 Å	R	1.″5	1.93×10^{35}
NGC 3631	0.28	6589/15 Å	6565/15 Å	0.″8	0.76×10^{34}
NGC 4321	0.28	6601/15 Å	6565/15 Å	0.″7–1.″0	3.78×10^{33}
NGC 5055	0.59	6576/20 Å	R	1.″5–1.″6	1.48×10^{34}
NGC 5364	0.59	6590/20 Å	R	1.″6	2.94×10^{35}
NGC 6764	0.28	6613/15 Å	6565/15 Å	0.″8	3.45×10^{34}
NGC 5985	0.59	66–/20 Å	R	1.″6	1.21×10^{35}
NGC 7479	0.28	6613/15 Å	6565/15 Å	0.″8	9.27×10^{34}

to isolate the order of interest (87th) containing Hα. A SITe 1024 × 1024 CCD with 24 μm pixels was used binned 2 × 2. The resulting spatial and spectral resolutions are 0.6″/pixel and 11.5 km s^{-1} (2.7 pixels *FWHM*). The spectra were calibrated in wavelength using observations of a ThAr lamp immediately following each object exposure. For all exposures, the slit was oriented N-S. The exposure time was always 1200 s. Once the bias was subtracted and the cosmic rays eliminated, one-dimensional spectra were extracted and calibrated in wavelength. All of this data reduction was done within IRAF.

2.3. Selection of HII regions and luminosity measurement

The HII regions were selected from among the brightest in each galaxy. Furthermore, they were chosen to be isolated in order to avoid problems with crowding and confusion in the measurement of the radii. The photometric data (radius and flux) for each HII region were obtained from published catalogues for NGC 157, NGC 925, NGC 3631, NGC 4321, NGC 6764, and NGC 7479 (Rozas et al. 1996a; Knapen et al. 1998; Rozas et al. 1999). For the other galaxies, for which no published HII region catalogues exist, the Hα fluxes were computed by summing all of the pixels that reasonably belonged to each HII region. In all cases, the intensity values used exceeded the local background noise by at least a factor of 2.5. Although diffuse Hα emission can affect the determination of radii and fluxes in HII regions, this is likely to be more important in faint HII regions, as opposed to the brightest ones chosen here. When computing the Hα fluxes for each HII region, the local sky background is subtracted, having been measured as spatially adjacent as practical. The uncertainty in HII region fluxes due to the background subtraction is less than 2% in all cases. For each HII region, the flux, position, and area are determined. The area is then converted to a radius, assuming that the HII regions are projections of a sphere on the sky. No correction is made to deconvolve the seeing profile since the HII regions are at least four times the size of the seeing profile. The luminosities and radii are given in Table 3.

3. Spectral analysis: profile extraction

To obtain the integrated spectrum of each HII region, we defined an aperture that corresponds to the radius given in Table 3 and centered this aperture on the flux peak. Given that the HII regions are isolated, there should be little error related to this procedure due to the lack of close neighbours. We checked whether our choice of aperture affected the kinematics measured for the principal component by systematically varying the aperture size, but we found that any variation was smaller than the measurement uncertainties.

The profiles were fit using the PROFIT task in GIPSY (Groningen Image Processing System), which can fit up to five Gaussian components to each profile and automatically determines the optimum number to fit. In Fig. 1, a selection of line profiles are shown along with the Gaussian components fit to each. In all cases, the decomposition into kinematic components is unambiguous.

Table 3. Hα luminosities and radii for the HII regions in our sample.

Region (galaxy)	log Hα	Rad (pc)	Region (galaxy)	log Hα	Rad (pc)	Region (galaxy)	log Hα	Rad (pc)
1 (NGC 925)	39.0525	280	15 (NGC 6764)	39.5258	370	29 (NGC 157)	39.7675	320
2 (NGC 925)	39.1758	320	16 (NGC 6764)	39.5486	340	30 (NGC 5055)	39.7764	250
3 (NGC 925)	39.2638	275	17 (NGC 3344)	39.5563	225	31 (NGC 7479)	39.8013	385
4 (NGC 3631)	39.2785	270	18 (NGC 6764)	39.5845	340	32 (NGC 5985)	39.8126	470
5 (NGC 5364)	39.2804	350	19 (NGC 5985)	39.5975	440	33 (NGC 7479)	39.8265	375
6 (NGC 5364)	39.2924	318	20 (NGC 157)	39.6109	310	34 (NGC 5985)	39.8469	410
7 (NGC 3631)	39.3167	260	21 (NGC 5364)	39.6138	340	35 (NGC 157)	39.8534	320
8 (NGC 4321)	39.3521	458	22 (NGC 5055)	39.6237	240	36 (NGC 6764)	39.8796	370
9 (NGC 5055)	39.3674	250	23 (NGC 3344)	39.6652	235	37 (NGC 157)	39.9046	320
10 (NGC 3631)	39.4036	355	24 (NGC 5985)	39.6743	410	38 (NGC 157)	39.9557	350
11 (NGC 3344)	39.4276	265	25 (NGC 5985)	39.6940	390	39 (NGC 7479)	39.9649	400
12 (NGC 3631)	39.4482	265	26 (NGC 157)	39.6982	265	40 (NGC 7479)	40.0328	400
13 (NGC 4321)	39.4848	335	27 (NGC 5055)	39.7145	250	41 (NGC 7479)	40.0462	385
14 (NGC 4321)	39.5036	200	28 (NGC 6764)	39.7512	370	42 (NGC 157)	40.0468	470
						43 (NGC 157)	40.0815	330

Most of the profiles are composed of three kinematic components. In only one case does the profile show two central peaks of comparable intensity, and the profile was fit with two Gaussian components. This object is not considered in the analysis that follows. In five additional cases, no secondary components were obvious, and the profiles were fit with a single Gaussian component. Other studies have found higher fractions of HII regions with line profiles composed of two comparable components. We have probably eliminated many of these cases in our sample by deliberately selecting HII regions that were clearly isolated. Arsenault & Roy (1996) analyzed 47 giant extragalactic HII regions and found 21% with profiles composed of two components of comparable intensity and 47% with profiles that were best fit by Voigt functions rather than by a Gaussian. We suspect that these objects with Voight profiles correspond to our cases of objects fit by three Gaussian components, namely an intense central component flanked by low intensity, high velocity components.

From the fit to the line profile for each HII region, we obtain the width of the intense, central component and, when present, the two fainter flanking components, which we denote as wings.

4. The luminosity-velocity dispersion relation

Once we measured the widths of the principal components, we corrected them for natural, thermal, and instrumental broadening to obtain what we denote as the non-thermal or turbulent width according to the following relation

$$\sigma_{\rm nt} = \left((\sigma_{\rm obs})^2 - (\sigma_{\rm n})^2 - (\sigma_{\rm t})^2 - (\sigma_{\rm ins})^2\right)^{1/2}. \quad (1)$$

The natural broadening is a constant for hydrogen, namely a width of 0.10 Å, which corresponds to 3 km s^{-1} (O'Dell & Townsley 1988). The thermal width, i.e., Doppler broadening, was determined from a standard procedure. For HII regions with temperatures of 5000 K, 10 000 K, and 15 000 K, Osterbrock (1989) provides Dopper widths of $\sigma_{\rm t}$ 6.4, 9.1, and 11.1 km s^{-1}, respectively. In the absence of more detailed temperature information for our sample, we adopted a uniform value of $\sigma_{\rm t} = 10\,{\rm km\,s^{-1}}$. Since this value enters the previous equation in quadrature, the error introduced by using a uniform value for $\sigma_{\rm t}$ is less than $2\,{\rm km\,s^{-1}}$ in all cases and will typically be less than $1\,{\rm km\,s^{-1}}$. This uncertainty is not worrisome since the uncertainty due to the remaining components in Eq. (1) is of order $5\,{\rm km\,s^{-1}}$. In all of the objects, $\sigma_{\rm nt}$ exceeds this overall uncertainty by a factor of several. The instrumental width was measured directly from the arc lamp taken immediately after the object exposure.

To construct the log $L_{\rm H\alpha}$ − log $\sigma_{\rm nt}$ diagram we must calculate the luminosity associated with the principal component of the line profile. Since the HII region luminosities, either from published catalogues or those measured here, are integrated over all kinematic components, we assume that the luminosity associated with the principal component corresponds to the fraction of the flux from this component in the line profile. In Fig. 2, we plot the Hα luminosity of the principal kinematic component as a function of its non-thermal velocity dispersion. Both of these values are given in Table 4.

This diagram shows that the velocity dispersion at a given luminosity is approximately constant as a function of luminosity, in contrast to what is found for studies considering the entire HII region population (Rozas et al. 1998; Relaño et al. 2005). All of the non-thermal velocity dispersions exceed 13 km s^{-1}, a canonical value for the sound speed in the interstellar medium (Smidth & Weedman 1970). The uncertainty in the non-thermal widths result from the signal-to-noise of the line profiles. In our case, these uncertainties are small, of order 2.5%, since we consider only bright HII regions and the widths are supersonic, significantly exceeding the instrumental resolution.

Rozas et al. (1998) found that, for the brightest HII regions, the lower envelope in the log $L_{\rm H\alpha}$ − log $\sigma_{\rm nt}$ plane was well-represented by a straight line. The slope found there was 2.6. Arsenault et al. (1990) found a similar slope for the surface brightness in the brightest HII regions, $\log F_{\rm H\alpha} = (2.57 \pm 0.49)\log\sigma_{\rm nt} - (17.21 \pm 0.39)$, $F_{\rm H\alpha}$ being the surface brightness in Hα. Likewise, Relaño et al. (2005) found, once they eliminated HII regions with non-thermal velocity dispersions below 13 km s^{-1}, that the lower envelope could be well-fit by a straight line, in their case $L_{\rm H\alpha} = (36.8 \pm 0.6) + (2.0 \pm 0.5)\log\sigma_{\rm nt}$, and conclude that only the HII regions near this envelope are approximately in virial equilibrium. In our case, a fit to all points leads to $L_{\rm H\alpha} = (35.6 \pm 0.4) + (2.87 \pm 0.2)\log\sigma_{\rm nt}$, which is in good agreement with the aforementioned studies, though having less dispersion. We therefore find that the fit considering only the principal component and the fit to the lower envelope have very similar slopes, which implies that the HII regions in our sample are also approximately in virial equilibrium.

In a given HII region, the thermal velocity width depends upon the temperature that, in turn, is a function of metallicity. The existence of metallicity gradients in galactic discs could then

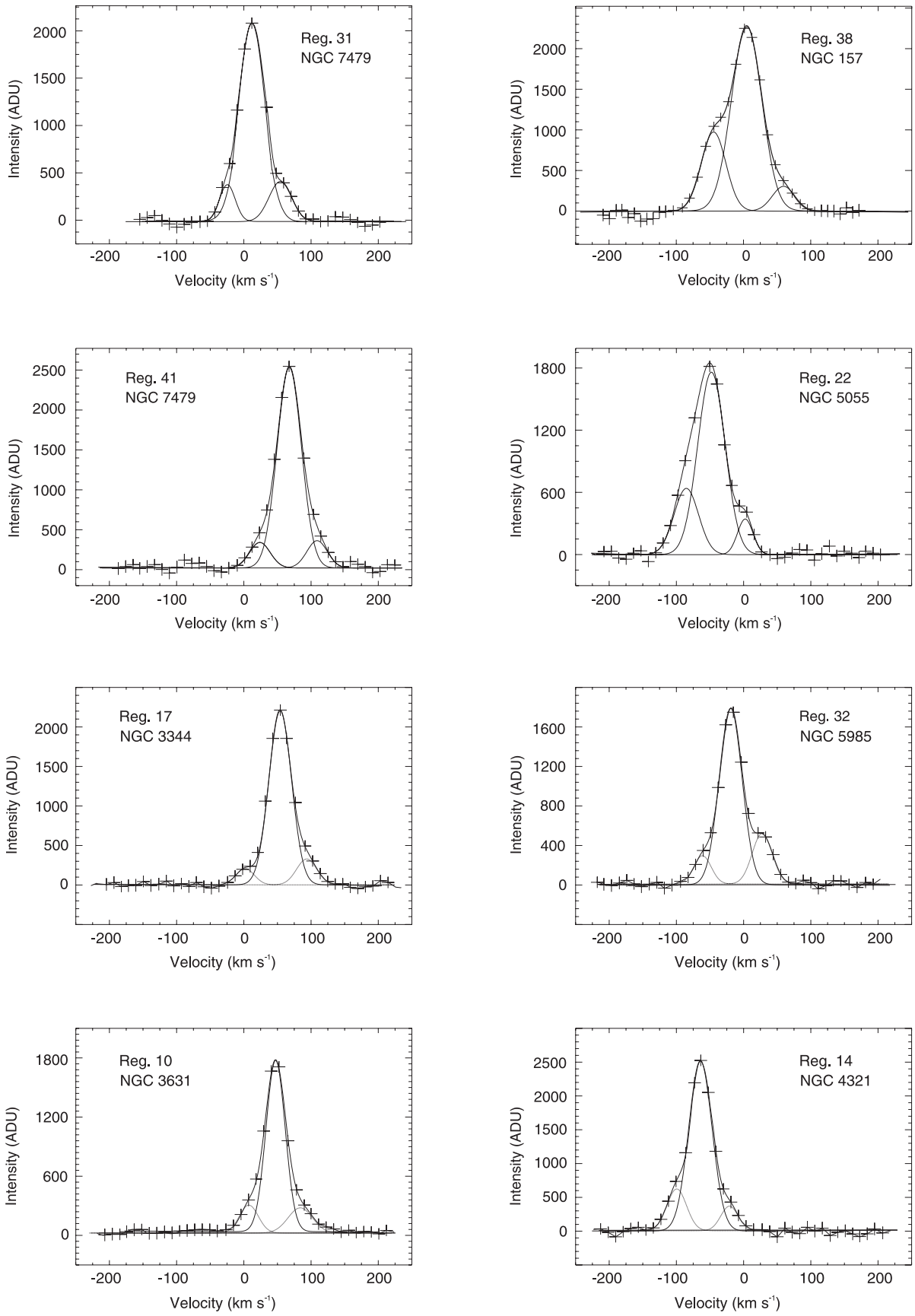

Fig. 1. Hα line profiles for some of the HII regions in our sample.

affect the $\log L_{\mathrm{H}\alpha} - \log \sigma_{\mathrm{nt}}$ relation. We have adopted a constant thermal velocity dispersion of 10 $\mathrm{km\,s^{-1}}$. Had we adopted temperatures of 5000 K or 15 000 K, the thermal velocity dispersions would have been 6.4 and 11.1 $\mathrm{km\,s^{-1}}$, respectively.

Table 4. Hα luminosity and turbulent velocity dispersion corresponding to the principal component for the HII regions in our sample.

Region (galaxy)	log Hα	σ_{nt}	Region (galaxy)	log Hα	σ_{nt}	Region (galaxy)	log Hα	σ_{nt}
1 (NGC 925)	39.0124	17.69	15 (NGC 6764)	39.4931	22.23	29 (NGC 157)	39.6845	27.66
2 (NGC 925)	39.1167	18.61	16 (NGC 6764)	39.4962	22.74	30 (NGC 5055)	39.6874	25.64
3 (NGC 925)	39.1851	22.85	17 (NGC 3344)	39.5563	26.74	31 (NGC 7479)	39.8013	28.39
4 (NGC 3631)	39.2279	20.13	18 (NGC 6764)	39.5013	26.05	32 (NGC 5985)	39.7323	26. 56
5 (NGC 5364)	39.2228	19.58	19 (NGC 5985)	39.5975	29.02	33 (NGC 7479)	39.7361	30.12
6 (NGC 5364)	39.2303	21.02	20 (NGC 157)	39.6109	25.31	34 (NGC 5985)	39.7702	28.70
7 (NGC 3631)	39.2867	18.60	21 (NGC 5364)	39.5421	20.46	35 (NGC 157)	39.8534	30.98
8 (NGC 4321)	39.2902	21.40	22 (NGC 5055)	39.5393	27.92	36 (NGC 6764)	39.8314	30.89
9 (NGC 5055)	39.3026	17.98	23 (NGC 3344)	39.5910	30.19	37 (NGC 157)	39.8323	30.19
10 (NGC 3631)	39.3624	19.58	24 (NGC 5985)	39.5455	21.77	38 (NGC 157)	39.8660	31.18
11 (NGC 3344)	39.3592	21.77	25 (NGC 5985)	39.5946	27.66	39 (NGC 7479)	39.9266	31.90
12 (NGC 3631)	39.4076	23.87	26 (NGC 157)	39.5871	24.88	40 (NGC 7479)	39.9648	30.89
13 (NGC 4321)	39.4027	20.70	27 (NGC 5055)	39.6382	31.04	41 (NGC 7479)	40.0392	28.70
14 (NGC 4321)	39.4501	22.85	28 (NGC 6764)	39.7512	28.20	42 (NGC 157)	39.9673	33.10
						43 (NGC 157)	40.0121	30.19

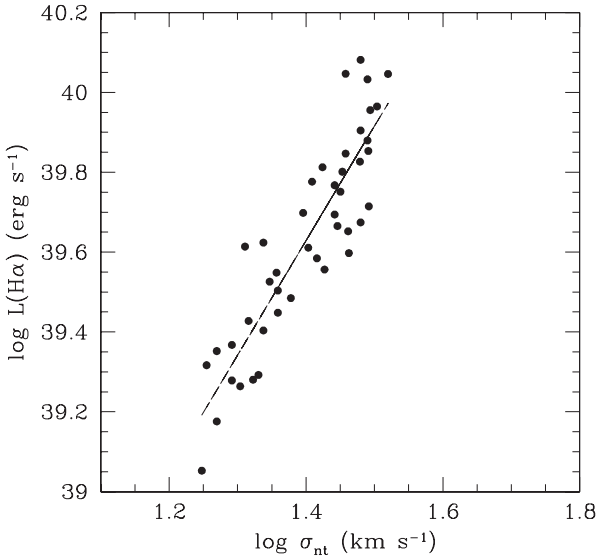

Fig. 2. The $\log L_{H\alpha} - \log \sigma_{nt}$ plane. Here the Hα luminosity is the luminosity corresponding to the principal component of the line profile for each HII region. σ_{nt} is the non-thermal velocity dispersion corresponding to this principal component.

Taking as an example an observed velocity width of 30 km s^{-1}, these thermal widths would imply non-thermal velocity dispersions of 27.0 and 25.4 km s^{-1}, respectively. This variation is within our error bars, so we do not expect metallicity gradients to affect our $\log L_{H\alpha} - \log \sigma_{nt}$ relation. This conclusion agrees with Relaño et al. (2005) who found that HII regions at a given galactocentric radius, and so presumably at similar metallicities, did not congregate in any given part of the $\log L_{H\alpha} - \log \sigma_{nt}$ plane, which led them to conclude that metallcity gradients had no important effect in this context.

5. HII region masses

We now compare the masses for our sample of HII regions based upon the virial theorem and upon their stellar and nebular luminosities. If the values from both methods are similar, we interpret this as indicating that the HII regions are near virial equilibrium.

Using the virial theorem, we compute virial masses for each HII region from

$$v^2 = \frac{GM_{vir}}{r_g} \quad (2)$$

where v is some characteristic internal velocity, for which we adopt $v = \sigma_{nt}$, G is the gravitational constant, r_g is a characteristic radius, and M_{vir} is the HII region mass. One problem in the determination of these masses is the uncertainty in choosing a characteristic radius. We have followed the criterion used by Relaño et al. (2005), adopting as our characteristic radius a value of one half of the total radius given in HII region catalogues. This is also consistent with Arsenault et al. (1990) who adopted the radius containing 40% of the total flux as their characteristic radius. Their choice was based upon the work of McCall et al. (1990), who demonstrated that the isophote containing 40% of the flux is a consistent measure of the size of HII regions and is not affected by the problems of detecting the edge of HII regions or of calibration. The virial masses of the HII regions in our sample computed in this way, M_{vir} are given in Table 5.

We can also estimate the mass of gas in an HII region by integrating over the volume (assumed spherical) and multiplying by the mass of atomic hydrogen

$$M_{reg} = (1 + Y)\, f \int \Phi^{1/2} \langle N_e \rangle_{rms} m_p dV \quad (3)$$

where Y is the helium mass fraction, for which we adopt 0.25, f is a factor that accounts for the fraction of neutral gas within the HII region, Φ is the filling factor, and $\langle N_e \rangle_{rms}$ is the rms electron density. Based upon the models of Giammanco et al. (2004), we adopt a neutral fraction of 10% since we have no way of obtaining a direct estimate of this fraction, and we are conscious of the uncertainty that this factor produces in the final results. In these models, the authors conclude that a fraction remains neutral due to internal inhomogeneities, an effect that affects all HII regions to a greater or lesser extent. We estimate $\langle N_e \rangle_{rms} = \sqrt{\langle N_e{}^2 \rangle}$ from the emission measure (EM) for each HII region, which is defined as the square of the electron density integrated along the line of sight

$$EM = \int_0^s N_e{}^2 ds \approx \langle N_e{}^2 \rangle \langle s \rangle \quad (4)$$

where $\langle s \rangle$ is the mean value of the length of the line of sight through an HII region averaged over its projected area (assumed equal to the radius). The emission measure is related to the surface brightness via (Spitzer 1978):

$$\frac{L_{H\alpha}}{\pi R^2} = h\nu_{H\alpha} \alpha^{eff}_{H\alpha}(H_0, T) \frac{N_p}{N_e} 2.46 \times 10^{17} \times EM \quad (5)$$

Table 5. Logarithmic Hα luminosity, emission measure, r.m.s. electron density, filling factor, virial mass, total mass of the HII region from the Hα emission, mass of the stellar content in the HII region, the fraction of the mass of the region that represents the virial mass and the turbulent kinetic energy of the HII region.

Region (galaxy)	log Hα (erg s^{-1})	EM (pc cm^{-6})	$\langle N_e \rangle_{rms}$ (cm^{-3})	Φ (10^{-4})	M_{vir} (10^6 $M_\odot$)	M_{reg} (10^6 $M_\odot$)	M_{star} (10^4 $M_\odot$)	M_{vir}/M_{reg}	K_{nt} (10^{51} erg)
1 (NGC 925)	39.0124	1300	2.1	2.4	10	1.7	2.2	5.8	5.3
2 (NGC 925)	39.1167	1300	2.0	2.2	13	2.2	2.9	5.9	7.6
3 (NGC 925)	39.1851	2300	2.9	4.6	17	2.9	3.5	5.8	15.1
4 (NGC 3631)	39.2279	2400	3.0	4.9	12	2.6	3.6	4.6	10.5
5 (NGC 5364)	39.2228	1900	2.4	3.2	14	2.9	3.8	4.8	11.1
6 (NGC 5364)	39.2303	1500	2.1	2.4	18	3.0	3.7	6.0	13.2
7 (NGC 3631)	39.3067	3000	3.3	5.8	10	3.1	4.0	3.2	10.7
8 (NGC 4321)	39.2902	1100	1.7	1.6	24	4.2	4.3	5.7	19.2
9 (NGC 5055)	39.3026	3600	3.8	7.9	9	3.4	4.4	2.6	11.0
10 (NGC 3631)	39.3624	2000	2.4	3.2	15	4.0	4.9	3.7	11.5
11 (NGC 3344)	39.3592	3600	3.6	7.1	14	3.0	5.3	4.6	14.2
12 (NGC 3631)	39.4076	4000	3.8	7.9	17	4.2	5.3	4.0	23.9
13 (NGC 4321)	39.4027	2700	2.9	4.6	16	4.7	5.7	3.4	20.1
14 (NGC 4321)	39.4501	7500	6.1	20.4	12	4.6	6.1	2.6	24.0
15 (NGC 6764)	39.4931	2500	2.6	3.7	21	5.2	6.4	4.0	25.7
16 (NGC 6764)	39.4962	2800	2.9	4.6	20	5.0	6.7	4.0	25.8
17 (NGC 3344)	39.5563	5400	6.7	24.0	20	8.5	10.1	2.3	60.8
18 (NGC 6764)	39.5013	3200	3.1	5.2	26	5.6	7.4	4.6	38.0
19 (NGC 5985)	39.5975	1700	2.7	4.0	44	10.4	6.9	4.2	87.6
20 (NGC 157)	39.6109	3900	5.0	13.7	23	11.4	9.2	2.0	73.0
21 (NGC 5364)	39.5421	3500	3.2	5.6	16	6.0	7.9	2.6	25.1
22 (NGC 5055)	39.5393	7000	5.4	16.0	21	6.2	8.1	3.4	48.3
23 (NGC 3344)	39.5910	7300	5.6	17.2	24	6.0	9.5	4.0	54.7
24 (NGC 5985)	39.5455	3300	2.9	4.6	18	7.0	9.5	2.5	33.2
25 (NGC 5985)	39.5946	2700	2.7	4.0	36	7.8	9.1	4.6	59.7
26 (NGC 157)	39.5871	7800	5.7	17.8	14	7.0	8.9	2.0	43.3
27 (NGC 5055)	39.6382	8000	5.6	17.2	27	7.4	10.0	3.6	71.3
28 (NGC 6764)	39.7512	3500	4.3	10.1	34	14.5	9.9	2.3	115.3
29 (NGC 157)	39.6845	5500	4.1	9.4	18	8.4	11.2	2.1	64.3
30 (NGC 5055)	39.6874	8000	5.6	17.2	18	7.4	11.4	2.4	48.6
31 (NGC 7479)	39.8013	3700	4.4	10.6	36	17.0	9.8	2.1	137.0
32 (NGC 5985)	39.7323	2800	2.4	3.2	39	9.7	12.5	4.0	68.4
33 (NGC 7479)	39.7361	4800	3.8	7.9	38	11.2	12.8	3.3	101.6
34 (NGC 5985)	39.7702	4000	3.1	5.2	39	10.2	13.4	3.8	84.0
35 (NGC 157)	39.8534	6000	6.1	20.4	35	18.6	10.9	1.9	178.5
36 (NGC 6764)	39.8314	5200	3.7	7.5	41	10.8	14.4	3.8	103.0
37 (NGC 157)	39.8323	7000	4.7	12.1	34	11.1	15.4	3.0	101.2
38 (NGC 157)	39.8660	7100	4.5	11.1	42	13.1	17.3	3.2	127.3
39 (NGC 7479)	39.9266	5500	3.7	7.5	47	13.6	17.7	3.4	138.4
40 (NGC 7479)	39.9648	6300	4.0	8.8	44	16.0	20.8	2.7	152.7
41 (NGC 7479)	40.0392	6800	4.2	9.7	36	15.5	21.3	2.3	127.7
42 (NGC 157)	39.9673	12000	6.5	23.1	35	14.0	21.3	2.5	153.4
43 (NGC 157)	40.0121	10500	5.7	7.8	33	10.6	23.3	3.1	96.6

where $\alpha^{\rm eff}_{H\alpha}(H_0, T)$ is the effective recombination coefficient for the Hα line at 10^4 K (e.g., Osterbrock 1974), $h\nu_{H\alpha}$ is the energy of Hα photons, R is the radius of the region, and $N_p/N_e = 1/1.1$ to account for ionized helium. From the luminosities and radii found in HII region catalogues, we obtain the emission measure from the above equation, which we then use to determine $\langle N_e \rangle_{rms}$. These rms electron densities and EM are given in Table 5. The EM and $\langle N_e \rangle_{rms}$ values agree well with those found by Kennicutt (1984) for extragalactic HII regions and later by Rozas et al. (1996b). Due to our selection criteria, our sample tends to include objects that are larger, more luminous, and less dense than galactic HII regions.

In order to infer the filling factor, we need to know the rms electron density averaged over a given region, which we have inferred from the emission measure, EM, and the electron density, N_e, measured directly within the ionized medium. In principle, this is possible using the ratio of intensities of the forbidden doublet $\lambda\lambda 6717, 6731$ Å of SII (see, e.g., Osterbrock 1974), but in practice these data are not available for the galaxies in our sample. To obtain approximate filling factors, we used a mean value of N_e found by Zaritsky et al. (1994) for 42 HII regions in a large sample of galaxies. These authors found a mean value of the ratio of 1.37 for the SII doublet intensity, corresponding to a value of 135 cm^{-3} for N_e.

The simple conceptual model assumed here is of an observed HII region containing a high density component which contributes all the observed emission flux, and occupies a fraction Φ, the filling factor, of the total volume, the rest of which contains a low density component which contributes negligibly. The filling factors, defined above, may be computed from (Danks & Meaburn 1971)

$$\Phi = \left(\frac{\langle N_e \rangle_{rms}}{N_e} \right)^2 . \quad (6)$$

The filling factors estimated for the HII regions in our sample are given in Table 5. From these filling factors, we compute the masses $M_{\rm reg}$ given in Table 5, calculated using Eq. (3).

In order to compare the virial masses with those derived via luminosities, we must account for the mass of stars formed within the HII regions. The total mass of stars may be obtained by integrating the initial mass function (IMF), which prescribes the number of stars formed as a function of stellar mass,

$$M_\star = \int_{m_{\rm l}}^{m_{\rm u}} m\varphi(m){\rm d}m \tag{7}$$

where $\varphi(m)$ is the IMF, which is normally represented as a power law in stellar mass: $\varphi(m) = Am^\alpha$, with $\alpha = -2.35$ for the Salpeter IMF (Salpeter 1955). To compute the stellar mass within an HII region, the normalization factor A, and the integration limits, i.e., the minimum and maximum stellar masses in the cluster, must be known. An estimate for A may be obtained by considering only the ionizing stars. Given the Hα luminosity, we may estimate the number of O5V stars required to produce this luminosity. Adopting a typical mass for this spectral type (Vacca et al. 1996), we may estimate the mass of ionizing stars, $M_{\rm i}$, within the HII region.

$$M_{\rm i} = \int_{m_{\rm i}}^{m_{\rm u}} Am^{-2.35}{\rm d}m. \tag{8}$$

If we then assume that the most massive ionizing star is of spectral type O3V and that stars later than O9V contribute less than 10% of the ionizing radiation, we obtain upper and lower limits of the integral of 51.3 $M_\odot$ and 22.1 $M_\odot$ (Vacca et al. 1996). Using these values in Eq. (8), we can estimate the value of A. Then, integrating Eq. (7) between the limits of 0.1 and 100 $M_\odot$, we can derive the total stellar mass within the HII region. This stellar mass is given in Table 5 as $M_{\rm star}$.

This means of estimating the stellar mass in HII regions is probably only indicative, since the IMF may differ from the Salpeter IMF, e.g., for NGC 346, Massey et al. (1989) find $\alpha = -2.9 \pm 0.3$ for 9–85 $M_\odot$ while Relaño et al. (2002) find $\alpha = -3.7 \pm 0.4$ for 24–54 $M_\odot$. Furthermore, the derivation of the ionizing stellar mass from the Hα luminosity is prone to underestimating the stellar mass, since some fraction of the ionizing radiation escapes the HII regions (Rozas et al. 1998; Beckman et al. 2000; Zurita et al. 2000). According to Relaño et al. (2002) the stellar mass derived in this way for NGC 346 represents only 60% of the stellar mass for spectral types O3V–O9V. Both of these issues complicate the calculation of the stellar masses in HII regions. The case of NGC 346 provides an illustrative example in this regard, as discussed by Relaño et al. (2002), who find that the stellar mass represents 0.17–0.44% of the gaseous mass, depending upon the lower limit used in Eq. (7) (0.1–1 $M_\odot$) while maintaining the upper limit fixed at 100 $M_\odot$. Even though these authors also find that the Hα luminosity underestimates the mass of ionizing stars, they conclude that the stellar mass nonetheless is less than 1% of the mass in gas. Even for an IMF slope as steep as $\alpha = -3.7$, Relaño et al. (2002) find that the stellar mass is only 4.7% of the mass in gas in NGC 346. Although it is evident that the uncertainties in computing the stellar mass are large, it is also evident that the stellar mass content in these HII regions represents only a very small fraction of the mass in gas and so its uncertainty will have no appreciable effect when comparing the gas masses computed using the Hα luminosity and the virial theorem.

6. Discussion

As noted earlier, Terlevich & Melnick (1981) proposed that the brightest giant extragalactic HII regions are virialized systems and derive the relation $\log {\rm H}\beta = 34.0 + 4.0 \log \sigma$. Subsequent studies, however, have not found the same result (Arsenault et al. 1990; Rozas et al. 1998; Relaño et al. 2002). Rozas et al. (1998) consider that these HII regions may be virialized, but argue that the deviation of the slope value from the theoretical prediction can be understood as the result of the brightest HII regions being density-bounded, in which case their Hα luminosities do not correspond to their total ionizing luminosities, but to a fraction substantially less. They introduce a gravitational radius, $r_{\rm g}$, parametrized as $r_{\rm g} = kL({\rm H}\alpha)^{1/n}$. For HII regions that are ionization-bounded, $r_{\rm g}$ should vary linearly with the volume, so that $n = 3$. In the case of HII regions that are density-bounded, n should take on a larger value since the luminosity grows more slowly due to the lack of matter. Based upon this hypothesis, they find $L({\rm H}\alpha) = k\sigma^{2n/(n-1)}$, which implies that virialized, density-bounded HII regions should follow a relation in the $\log L - \log \sigma$ plane with a shallower slope than the theoretically predicted value of 4. The slope of 2.87 that we find for this relation corresponds to value of $n = 3.3$, a value closer to that predicted by the virial theorem.

In Table 5, the virial mass, $M_{\rm vir}$ is generally larger than the mass based upon the Hα luminosity. $M_{\rm vir}/M_{\rm reg}$ varies from 2–6, meaning that the HII regions considered here are close to being in virial equilibrium. In contrast, those observed by Relaño et al. (2005) and which are not near the upper envelope have values of $M_{\rm vir}/M_{\rm reg}$ that vary from 7–15. As noted earlier, strict virial equilibrium is unlikely to hold at any time during the evolution of an HII region. Ionization, stellar winds (Dyson 1979), supernova explosions (Skillman & Balick 1984), or champagne flows (Tenorio-Tagle 1979) will all affect, and eventually dominate, the kinematics. Even the HII regions in our sample usually display symmetric high velocity kinematic components whose properties will form the basis of a future study (Fig. 1, Sect. 3). Given the similarity of the properties of the blue and red high velocity components, it is natural to interpret them as the kinematic signature from a coherent structure, of which the simplest is an expanding internal shell. If so, their true kinematic signature in spatially-unresolved kinematic observations will be a top-hat profile (e.g., Gesicki & Ziljstra 2000) that will perturb the properties measured for the principal kinematic components considered here. As a result, the true line width of the principal component will be overestimated, which, in turn, will lead to an overestimate the true virial mass presented in Table 5, a topic that we plan to address via future modelling. Considering this effect, the true ratios of virial and luminous masses, $M_{\rm vir}/M_{\rm reg}$, will be somewhat lower than the values tabulated in Table 5.

Clearly, then, the line width observed in an HII region is due to the superposition of the velocity fields resulting from different physical processes, of which gravitation is only one. In general, the energy to sustain the velocity fields other than that due to gravity will be injected by individual events, the winds of massive stars, and supernovae, and the average profile will be a superposition of the velocity fields from these events on the general background dispersion of the HII region. The fraction of the emission observed that comes from sources of high velocity dispersion, will depend upon the fraction of the total luminous gas that participates in these events and the damping time for gaseous expansion within a given region. Both of these should fall with increasing gas mass, i.e. with increasing HII region luminosity. In the limit where the fraction of gas with high

velocity dispersion tends to zero, we should observe an HII region with virialized internal motions reflected in the velocity dispersion. This general trend is observed in the ratios of virial and luminous masses, $M_{\rm vir}/M_{\rm reg}$, in Table 5 in the sense that the most luminous HII regions also have the smallest values of this ratio.

In general, therefore, the velocity dispersions of HII regions are not the result of virial equilibrium alone, other processes must contribute in most cases, but there is a small subsample of the HII region population where the condition of virial equilibrium is nearly fulfilled. It should be possible to pick out these HII regions with velocity dispersions resulting from virial equilibrium given measurements of the dispersion, σ, for the complete population of HII regions in a galaxy.

7. Conlusions

We have analyzed Hα line profiles in a sample of isolated, bright giant HII regions in ten spiral galaxies. These line profiles have been decomposed into Gaussian components. Our principal findings are

- Of our initial sample of 43 HII regions, in the great majority (37) the brightest, principal component is accompanied by low intensity components with higher velocities.
- We find a relation between the Hα luminosity, L(Hα), and the non-thermal velocity dispersions, $\sigma_{\rm nt}$ such that $\log L(\mathrm{H}\alpha) = (35.6\pm0.4)+(2.87\pm0.2)\log\sigma_{\rm nt}$, where L(Hα) is the fraction of the Hα luminosity corresponding to the principal component. The slope has a value below the value of 4 predicted theoretically for virial equilibrium, in agreement with the finding in Beckman et al. (2000) that bright HII regions are generally density-limited and so an important fraction of their ionizing photons escape without contributing to their Hα luminosities.
- We calculate the stellar mass within each HII region, finding that it is a small fraction, less than 1–2%, of the total mass.
- We compare the masses of gas calculated from the virial theorem and directly from the Hα luminosity. Although the two masses do not coincide, they are generally similar. This result shows that those HII regions may well be close to virial equilibrium, and that non-gravitational processes do not completely dominate the broadening of the principal kinematic component, especially at the highest luminosities.

Acknowledgements. M.G.R. and J.A.L. acknowledge financial support from CONACyT grant 43121-E as well as DGAPA grants IN112103. We acknowledge the work of G. Melgoza and S. Monroy as telescope operators during the acquisition of these data.

References

Arsenault, R., & Roy, J. R. 1986, AJ, 92, 567
Arsenault, R., & Roy, J. R. 1988, A&A, 201, 199
Arsenault, R., Roy, J.-R., & Boulesteix, J. 1990, A&A, 234, 23
Beckman, J. E., Rozas, M., Zurita, A., Watson, R. A., & Knapen, J. H. 2000, AJ, 119, 2728
Castañeda, H. O., Vilchez, J. M., & Copetti, M. 1990, ApJ, 365, 164
Castor, J., McCray, R., & Weaver, R. 1975, ApJ, 200, L107
Danks, A. C., & Meaburn, J. 1971, Ap&SS, 11, 398
Dyson, J. E. 1979, A&A, 73, 132
Gallagher, J. S., & Hunter, D. 1983, ApJ, 274, 141
Giammanco, C., Beckman, J. E., Zurita, A., & Relaño, M. 2004, A&A, 424, 877
Gesicki, K., & Ziljstra, A. A. 2000, A&A, 358, 1058
Hippelein, H. H. 1986, A&A, 160, 374
Kennicutt, R. C., Jr. 1998, ARA&A, 36, 189
Knapen, J. H. 1998, MNRAS, 297, 255
Leitherer, C., Schaerer, D., Goldader, J. D., et al. 1999, ApJS, 123, 3
Massey, P., Parker, J. W., & Garmany, C. D. 1989, AJ, 98, 1305
McCall, M. L., Hill, R., & English, J. 1990, AJ, 100, 193
Meaburn, J., Blundell, B., Carling, R., et al. 1984, MNRAS, 210, 463
Meaburn, J., Lpez, J. A., Gutirrez, L., et al. 2003, Rev. Mex. Astron. Astrofis., 39, 185
Melnick, J. 1977, AJ, 213, 15
ODell, C. R., & Townsley, L. K. 1988, A&A, 198, 283
Osterbrock, D. E. 1989, Astrophysics of Gaseous Nebulae and Active Galactic Nuclei (Mill Valley: University Science Books)
Relaño, M., Peimbert, M., & Beckman, J. E. 2002, ApJ, 564, 704
Relaño, M., Beckman, J. E., Zurita, A., Rozas, M., & Giammanco, C. 2005, A&A, 431, 235
Roberts, M. S., & Haynes, M. P. 1994, ARA&A, 32, 115
Roy, J.-R., Arsenault, R., & Joncas, G. 1986, ApJ, 300, 624
Rozas, M., Beckman, J. E., & Knapen, J. H. 1996a, A&A, 307, 735
Rozas, M., Knapen, J. H., & Beckman, J. E. 1996b, A&A, 312, 275
Rozas, M., Sabalisck, N., Beckman, J. E., & Knapen, J. H. 1998, A&A, 338, 15
Rozas, M., Zurita, A., Heller, C. H., & Beckman, J. E. 1999, A&AS, 135, 145
Salpeter, E. E. 1955, ApJ, 121, 161
Skillman, E., & Balick, B. 1984, ApJ, 280, 580
Smith, M., & Weedman, D. 1970, AJ, 161, 33
Spitzer, L. 1978, Physical Processes in the Interestellar Medium (New York: J. Wiley & Sons)
Tenorio-Tagle, G. 1979, A&A, 71, 59
Terlevich, R., & Melnick, J. 1981, MNRAS, 195, 839
Vacca, W. D., Garmany, C. D., & Shull, M. 1996, ApJ, 460, 914
Yang, H., Chu, Y.-H., Skillman, E. D., & Terlevich, R. 1996, AJ, 112, 146
Zaritsky, D., Kennicutt, J. R., & Huchra, J. P. 1994, ApJ, 420, 87
Zurita, A. 2001, Ph.D. Thesis, Univ. La Laguna
Zurita, A., Rozas, M., & Beckman, J. E. 2000, A&A, 363, 9